Carbon 143 (2019) 752–761

Contents lists available at ScienceDirect

Carbon

journal homepage: www.elsevier.com/locate/carbon

Elastomer-like deformation in high-Poisson's-ratio graphene allotropes may allow tensile strengths beyond theoretical cohesive strength limits

Hao Sun [a], Sankha Mukherjee [b], Zhe Shi [b, c], Chandra Veer Singh [a, b, *]

[a] Department of Mechanical and Industrial Engineering, University of Toronto, Toronto, ON, M5S 3G8, Canada
[b] Department of Materials Science and Engineering, University of Toronto, Toronto, ON, M5S 3E4, Canada
[c] Department of Materials Science and Engineering, Massachusetts Institute of Technology, Cambridge, MA, 02139, USA

ARTICLE INFO

Article history:
Received 17 October 2018
Received in revised form
25 November 2018
Accepted 26 November 2018
Available online 27 November 2018

ABSTRACT

Phenomenological theories of deformation in brittle solids generally envisage fracture under tension as the breaking of atomic bonds perpendicular to the fracture plane, thereby ignoring the role of bond rotation. Using density functional theory calculations, we found that during the early stage of the uniaxial tension of graphene allotropes with high Poisson's ratios, bond rotation effectively lessens bond stretch and increases the fracture strain. Specifically, in the deformation of an allotrope, Gr10, with a Poisson's ratio of 0.8, bond rotation results in an S-shaped stress-strain curve, akin to those of elastomers. Moreover, the tensile strength (σ_{th}) and the Young's modulus (E) of Gr10 exceed the theoretical cohesive strength limit $\sigma_{th} \approx E/10$, reaching $\sigma_{th} \approx E/1.7$. However, a universal relationship between bond lengths and charge density distribution along bond paths was found to be suitable for all carbon-carbon covalent bonds. Consequently, all carbon-carbon bonds obey a common shape of bond-force vs. bond-strain curve, with bond strength, S, and bond stiffness, K, following $S \approx K/9$; hence, $\sigma_{th} \approx E/10$ remains valid for the low-Poisson's-ratio graphene allotropes whose deformation is dominated by bond stretch. Overall, we suggest the trade-off between bond stretching and bond rotation can be utilized to enhance the fracture strain of two-dimensional carbon structures.

1. Introduction

According to Griffth's theory of brittle fracture [1], a brittle solid fractures by the breaking of atomic bonds perpendicular to the fracture plane. In this scenario, the fracture strength of the atomic bond within a brittle solid devoid of any defects is defined as the theoretical cohesive strength (σ_{th}) of the solid. According to the theory proposed by Griffth [1], Orowan [2], and others [3,4], σ_{th} is approximately equal to $E/10$, where E is Young's modulus. Of most traditional engineering materials, however, the measured tensile strength is usually lower than $E/50$ [5] due to the omnipresent structural defects (such as impurities, cracks, voids). The local magnification of stress intensity near these defects [1] initiates crack propagation at an applied stress much smaller than σ_{th}. Nonetheless, σ_{th} is still used to determine the fracture behavior at crack tips [3,6], dislocation core radius in crystals [7,8], and the breaking point of coherency at a particle-matrix interface in alloys [9], where the critical structure involved in these calculations is so small that no defect is present inside.

Since the probability of finding defects inside a material reduces as the size of the sample decreases, σ_{th} can also be measured experimentally when the sample size is small enough to avoid any defects. One commonly used experimental technique to measure σ_{th} is the atomic force microscope nanoindentation of monolayer 2D materials [10]. By suspending 2D materials over open holes with diameters ranging from 1 to 3 μm, one-atom-thick membranes with diameters less than 3 μm are obtained, defect-free. Using similar techniques, researchers have measured a tensile strength of 130 GPa of graphene, close to $E/8$ [10], 23 GPa of monolayer MoS_2, reaching $E/11$ [11], and 24.7 GPa of monolayer graphene oxide films, approximately equal to $E/15$ [12].

Inspired by the experimental results on 2D materials, a substantial amount of research has tried to use density functional

* Corresponding author. Department of Mechanical and Industrial Engineering, University of Toronto, Toronto, ON, M5S 3G8, Canada.
E-mail address: chandraveer.singh@utoronto.ca (C.V. Singh).

https://doi.org/10.1016/j.carbon.2018.11.079
0008-6223/

theory (DFT) simulations to study more 2D materials exhibiting σ_{th} close to $E/10$. For example, DFT simulations predicted an ideal strength $\sim E/11$ for graphene [13], $\sim E/12$ for graphene oxide [12], $\sim E/13$ for borophene [14], and $\sim E/13$ for g-GeC [15]. Specifically, a 2D structure, stanene, is found to possess σ_{th} up to $\sim E/7$, breaking the traditional limit $E/10$ [16,17]. However, it is still unclear what is the fundamental reason for such a breakthrough of the theoretical strength limit in 2D materials. Furthermore, previous research on the structure-mechanical property relations of graphene allotropes found that not only bond stretch, angles between different bonds also change during uniaxial deformation [18,19]. A larger rotation angle is found in graphene allotropes with higher Poisson's ratios and lower area densities of atoms, leaving more free space for bond rotation. Unfortunately, the effect of bond rotation is absent in the Griffth theory of brittle fracture, with its influence on the theoretical cohesive strength unknown.

In this study, first-principles density functional theory (DFT) calculations were conducted to investigate the fundamental deformational mechanisms underpinning the exceedance of the theoretical cohesive strength of 2D materials. First, we simulated the uniaxial deformation of carbon-based 2D structures and stanene, with Poisson's ratios ranging from 0.16 to 0.8, to study the influence of bond rotation on the mechanical properties of graphene allotropes. Next, to gain physical insights in the fracture strength of carbon-carbon covalent bonds, we investigated the tensile deformation of different carbon-carbon covalent bonds and analyzed the evolution of charge density distribution during bond stretching.

2. Methodology

All simulations were performed using the Quantum-ESPRESSO package [20]. A pseudopotential with Perdew-Berke-Ernzerhof (PBE) exchange-correlation functional [21] was used along with Monkhorst–Pack k-point mesh [22]. The kinetic energy cut-off for wavefunctions and charge density are 60 Ry and 480 Ry, respectively. Five representative 2D structures were studied, including graphene, planar C4 Octagraphene (OcGr) [23], Gr11 [24], 18,18,18-graphene (Gr10) [25], and stanene (Fig. 1(b)), with Poisson's ratios spanning from 0.16 of graphene to 0.8 of Gr10. The unit cells of each structure are illustrated in Fig. 1(b). There was a 20 Å vacuum in the out-of-plane direction to avoid any inter-layer interactions. Each system was initially relaxed using a conjugate gradient minimization method. The convergence threshold on the self-consistent field (SCF) procedures, the total energy for ionic minimization between two consecutive scf steps, and the Hellmann Feynman force on each atom are 1.0×10^{-6} Ry, 1.0×10^{-4} Ry, and 0.001 Ry/Bohr, respectively.

Strain-controlled uniaxial tensions were performed on the unit cells of different structures. Strains were applied by dilating the unit cells along the loading direction and an equal affine transformation to the atomic positions. The deformed conformation was then subjected to an energy minimization routine to obtain its ground-state configuration. During the relaxation, the cell dimensions in the tensile axis were kept constant to preserve the overall strain. It is important to note that in most of previously reported DFT simulations [13,15,16,18,19,26–28], the cell dimension in directions perpendicular to the loading axis was kept constant, prohibiting any dimensional changes in the transverse direction during relaxation. This boundary condition is against the experimental uniaxial tension, in which the transverse surfaces are usually kept free, allowing for the Poisson effect, the phenomenon in which a material tends to compress in directions perpendicular to the direction of tension (Fig. 1(a)). It is in the free-boundary boundary condition that the Young's modulus of the material is defined as the initial slope of the stress-strain curve [1–4], $E = \lim_{\varepsilon \to 0} d\,\sigma(\varepsilon)/d\varepsilon$. Thus, to mimic a more realistic scenario, the free-boundary condition was applied in our simulations. The influence of boundary condition on the uniaxial deformation is discussed in detail in Supporting Information Section 1.

3. Results and discussion

3.1. Stress-strain responses

The uniaxial stress-strain curves of graphene, OcGr, Gr11, Gr10, and stanene are shown in Fig. 1(c). They are non-linear from the beginning of the loading. For graphene, OcGr, Gr11, and Stanene, the slope of their stress-strain curves decreases with strains, reaching zero when the stress increases to their ultimate tensile strength (UTS). Different from other structures, however, the stress-strain curve of Gr10 has an increasing slope up to a strain of 0.17 and then the slope decreases, resulting in an S-shape stress-strain curve and the largest fracture strain among all the five structures. Besides, the deformation mechanisms of these structures are illustrated in Fig. 1(d). During the deformation, the unit cell dilates in the loading axis but shrinks in the transverse direction: the dilation is accommodated by bond stretch; rotation of bonds inclined to the loading axis introduces contraction in the transverse direction. When stretched to the fracture strain, all structures fracture by the breaking of bonds undertaking the most substantial elongation, bonds that are usually parallel to the loading axis as described in the Griffth theory of brittle fracture [1].

According to the Griffth theory of brittle fracture, the σ_{th} of any brittle material is approximately equal to $E/10$, where E is the Young's modulus. Because all the models used here are devoid of any defects, σ_{th} is the UTS of the stress-strain curve in Fig. 1(c). In our simulations, the E/σ_{th} for graphene and stanene are 8.9 and 8.21, respectively, comparable to the $E/10$ limit [25]. Previous DFT simulations also got $\sim E/12$ for graphene oxide [12], $\sim E/13$ for borophene [14], and $\sim E/13$ for g-GeC [15], all close to the approximation $E/10$. Furthermore, the atomic force microscope nanoindentation of monolayer 2D materials suspended over open holes measured a σ_{th} of $E/8$ [10] for graphene, $E/11$ [11] for MoS_2, and $E/15$ [12] for graphene oxide. However, this limit is not valid for OcGr, with E/σ_{th} reducing to 5.8. Specifically, E/σ_{th} of Gr10 even plummets to 1.7, much lower than the traditional approximation $E/\sigma_{th} \approx 10$.

The low E/σ_{th} for Gr10 is attributed to its unique S-shape stress-strain curve, with a significantly reduced Young's modulus but an undiminished UTS. This S-shape stress-strain curve bears some resemblances to the deformation of elastomers such as polyurethane [29,30], of which the stress-strain curve is also characterized by elastic moduli increasing with strains (Fig. 1(e)). In addition, though non-linear, the deformation of polyurethane up to the UTS point is entirely reversible, analogous to that of Gr10. With an irregular structure, weak intermolecular attractive forces, and flexible polymer chains, polyurethane can be easily stretched by the straightening of amorphous polymer chains from their curled positions into partially extended conformations. By the re-orientation and unfolding of polymer chains, external deformation can be accommodated with little additional lengthening attributed to the more difficult covalent-bond stretching, which is responsible for the increasing slope of its stress-strain curve as strain increases. However, while polyurethane is famous for its considerable nonlinear elastic strain (over 1000%) [29,30], the fracture strain for Gr10 is only 0.33; nonetheless, 0.33 is still the largest fracture strain among all the five structures.

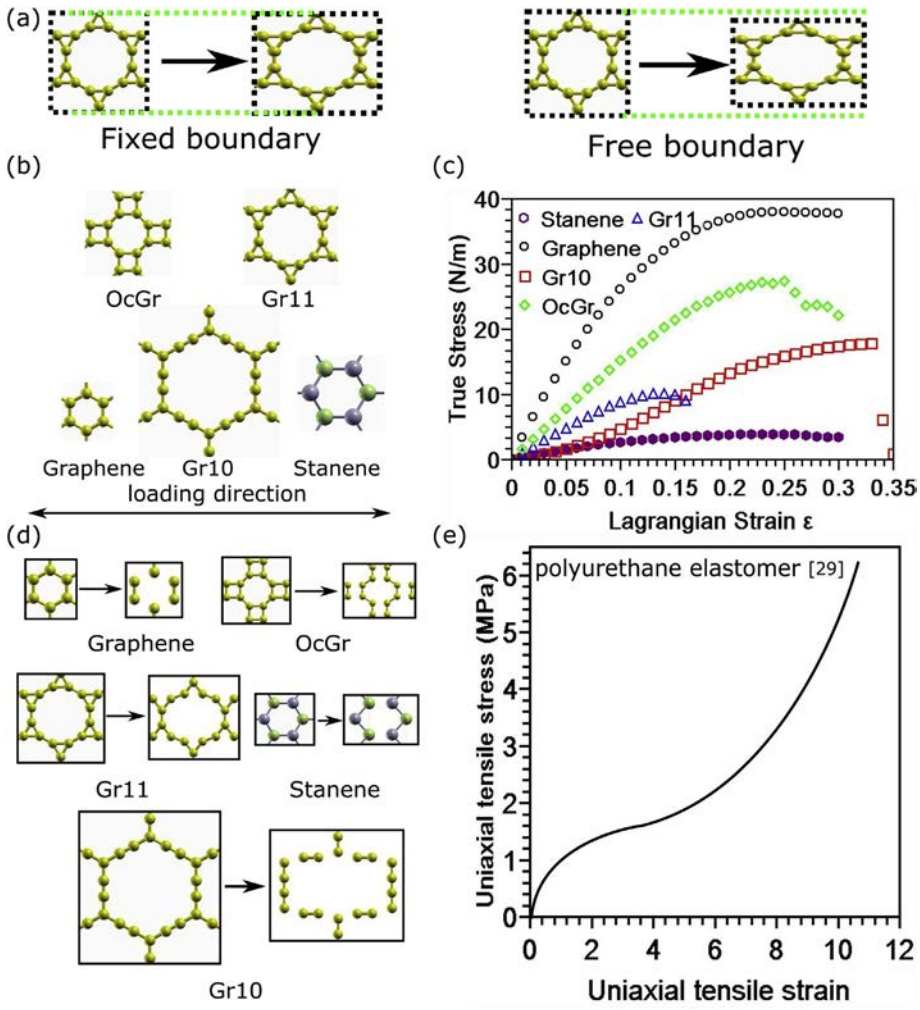

Fig. 1. The unique stress-strain curve of high-Poisson's-ratio graphene allotropes in free-boundary uniaxial tension. (a) The uniaxial loading of Gr11 under the free-boundary and fixed-boundary conditions. (b) The atomic topologies of four graphene allotropes and stanene. Atoms colored by green in stanene belong to a different plane with the other blue atoms. (c) The free-boundary uniaxial stress-strain curves of the five representative structures. (d) The atomic conformation at fracture strain. The unit cell of each structure is illustrated by a black rectangle. (e) The uniaxial tensile stress-strain curve of polyurethane elastomer [28]. (A colour version of this figure can be viewed online.)

3.2. Deformational mechanisms underpinning elastomeric stress-strain response

Despite the unique shape of its stress-strain curve, Gr10, like all the other structures, can only deform by bond stretch and bond rotation. Besides introducing contraction in the transverse direction, bond rotation also undertakes a part of the elongation in the uniaxial direction, akin to the lessening of covalent bond stretching in polyurethane by the unfolding of molecular chains. To investigate the interaction between bond strain and bond rotation in graphene allotropes, we plotted in Fig. 2(b) the rotation degree $\Delta\theta$ of seven bond angles and in Fig. 2(c) the strain of five bonds: the angles are labeled by numbers in Fig. 2(a); the bonds investigated here are colored by blue. As shown in Fig. 2(b), $\Delta\theta$ of $\theta5$ and $\theta6$ in Gr10 at each strain value is larger than that of any other angles, with $\Delta\theta$ of $\theta1$ in graphene the lowest. In contrast to bond rotation, at each applied strain value, bond strain is the lowest in Gr10 and the largest in graphene (Fig. 2(c)). Thus, when more bond rotation accommodates the external deformation, less contribution from bond stretching is required. Since less force is needed to rotate a bond than to stretch a bond [19], the enhancement in bond rotation decreases the elastic modulus, especially in Gr10. However, as the applied strain increases, the slope of $\Delta\theta(\varepsilon)$ decreases, reflecting a diminishing effect of bond rotation. On the other hand, all the relations between the bond strain and the applied strain have increasing slopes, indicating an intensifying effect of bond stretch. Accordingly, as the applied strain increases, bond rotation becomes less effective in undertaking external deformation; thus, more deformation is accommodated by bond stretch, resulting in a strain-hardening curve of Gr10. Finally, when the effect of bond stretch overtakes that of bond rotation, Gr10 behaves like the other structures, deforming with a strain-softening behavior until fracture.

To further investigate the deformation mechanism of the atomic ring in graphene allotropes, we separate the strain of the largest atomic ring into a strain due to bond rotation ($\varepsilon^{\theta}_{\mathrm{ring}}$) and a strain due to bond stretching ($\varepsilon^{\mathrm{l}}_{\mathrm{ring}}$), a strategy which was implemented in a previous study of polyimide [31]. $\varepsilon^{\theta}_{\mathrm{ring}}$ and $\varepsilon^{\mathrm{l}}_{\mathrm{ring}}$ are defined as follows

$$\varepsilon^{\theta}_{\mathrm{ring}} = \frac{\sum_{i=1}^{n} l_i^0\left(\cos\theta_i^1 - \cos\theta_i^0\right)}{L_0} \qquad \varepsilon^{\mathrm{l}}_{\mathrm{ring}} = \frac{\sum_{i=1}^{n} \cos\theta_i^0\left(l_i^1 - l_i^0\right)}{L_0} \tag{1}$$

Where l_i^0 and θ_i^0 are the initial bond length and bond angle; l_i^1 and

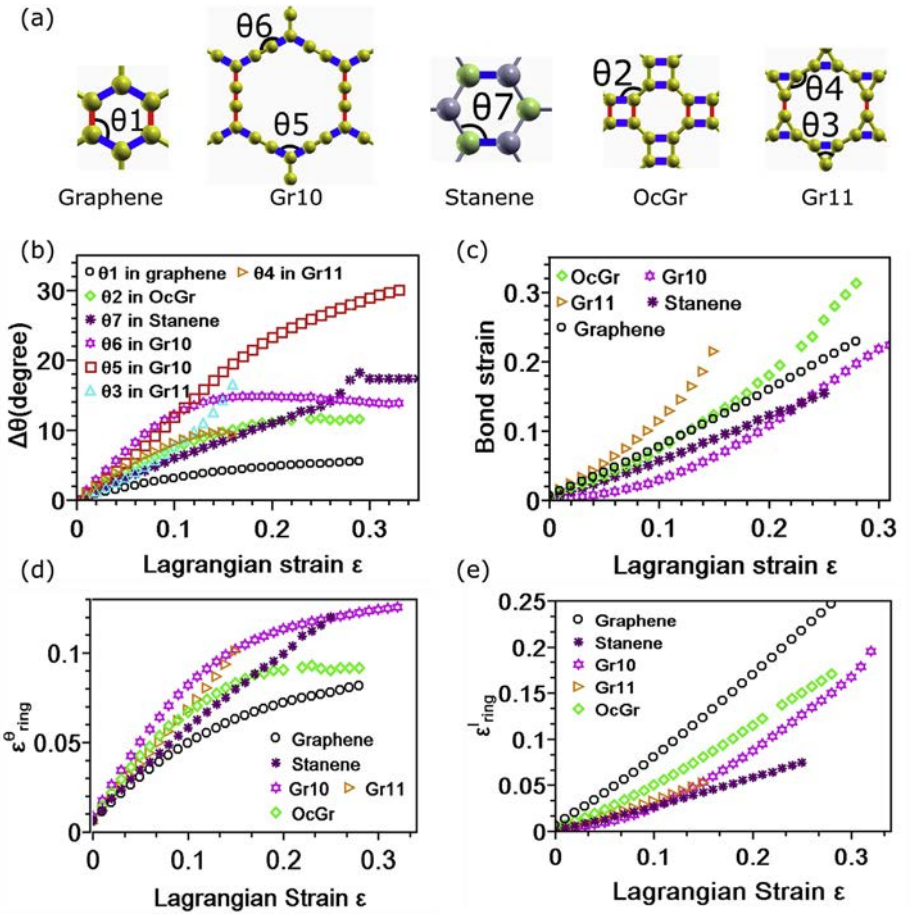

Fig. 2. Competition between bond stretch and bond rotation in uniaxial tension of graphene allotropes and stanene. (a) Atomic topologies of four graphene allotropes and stanene. (b) The relation between applied strains and rotation degree $\Delta\theta$ of seven angles labeled in Fig. 2(a). (c) The relation between applied strains and the strains of bonds colored by blue in Fig. 2(a). (d) The relation between $\varepsilon^{\theta}_{\mathrm{ring}}$ and applied strain. (e) The relation between $\varepsilon^{l}_{\mathrm{ring}}$ and applied strain. (A colour version of this figure can be viewed online.)

θ_i^1 is the corresponding bond length and bond angle after the structure is deformed; L_0 is the initial dimension of the atomic ring in the tensile axis, and n is the total number of bonds within the atomic ring. The evolution of $\varepsilon^{\theta}_{\mathrm{ring}}$ and $\varepsilon^{l}_{\mathrm{ring}}$ with the applied strain is plotted in Fig. 2(d) and (e), respectively. Generally, at small strains, bond rotation is favorable, and $\varepsilon^{\theta}_{\mathrm{ring}}$ is always larger than $\varepsilon^{l}_{\mathrm{ring}}$. However, in the large loading region, the deformation resistance to bond rotation becomes larger than that to bond stretching; hence, the relationship between $\varepsilon^{\theta}_{\mathrm{ring}}$ and the applied strain levels off, while $\varepsilon^{l}_{\mathrm{ring}}$ increases steeply with strain. Additionally, like the relationship between $\Delta\theta(\varepsilon)$ and the applied strain plotted in Fig. 2(b), $\varepsilon^{\theta}_{\mathrm{ring}}$ is the largest in Gr10 and decreases with Poisson's ratios; analogous to the bond strain plotted in Fig. 2(c), the $\varepsilon^{l}_{\mathrm{ring}}$ is the lowest in Gr10 and increases as the Poisson's ratio decreases. Overall, the analysis $\varepsilon^{\theta}_{\mathrm{ring}}$ and $\varepsilon^{l}_{\mathrm{ring}}$ confirms that the bond-rotation effect becomes essential in high-Poisson's-ratio graphene allotropes, and that the enhancement of bond rotation would release bond strain.

The competition between bond rotation and bond stretch is also reflected in the area expansion rate. Since bond rotation is mainly accounted for the contraction in the transverse direction, the area expansion rate of high-Poisson's-ratio graphene allotropes, with more bond rotation occurring during deformation, could be smaller than that of low-Poisson's-ratio graphene allotropes. For example, as shown in Fig. 3(a), at each strain value, graphene has the highest area expansion rate due to its lowest Poisson's ratio. OcGr and Gr11 have similar area expansion rate due to their almost equivalent Poisson's ratios (0.64 and 0.6). However, the area of the unit cell of Gr10 even shrinks to 99% of the initial unstressed area at a strain of 0.12. As the bond-rotation effect is gradually overwhelmed by the bond-stretch effect, the area increases to the original value at a strain of 0.17, the same strain that divides the strain-hardening part and the strain-softening part of the S-shape stress-strain curve of Gr10.

Despite having high Poisson's ratios, OcGr does not exhibit the unique S-shape stress-strain curve but rather the typical strain softening behavior (Fig. 1(c)). A major reason for that is due to its smaller carbon rings than that in Gr10, its Poisson's ratios (~0.6), notwithstanding higher than that of graphene (0.16), are still lower than that of Gr10 (0.8). Thus, the influence of bond rotation in OcGr is less pronounced than in Gr10. For example, the E/σ_{th} of OcGr (~5.8), although less than 10, is still higher than that of Gr10 (~1.7). Moreover, as bond stretch accounts for elongation in the tensile axis while bond rotation introduces contraction in the transverse direction, the ever-expanding area of the unit cell of OcGr during deformation (Fig. 3(a)) indicates the bond-stretch effect surpasses the bond-rotation effect. Hence, due to the dominance of bond stretch, the shape of its stress-strain curves is still conventional. Only when the Poisson's ratio reaches 0.8 in Gr10 could bond rotation finally overwhelm bond stretch. The resulting quantitative reduction of E/σ_{th} is so significant (~1.7) that even qualitative changes emerge, such as the S-shape stress-strain curve (Fig. 1(c)) and the areal shrinkage at small strains (Fig. 3(a)).

Underpinning the contraction in the transverse direction is a

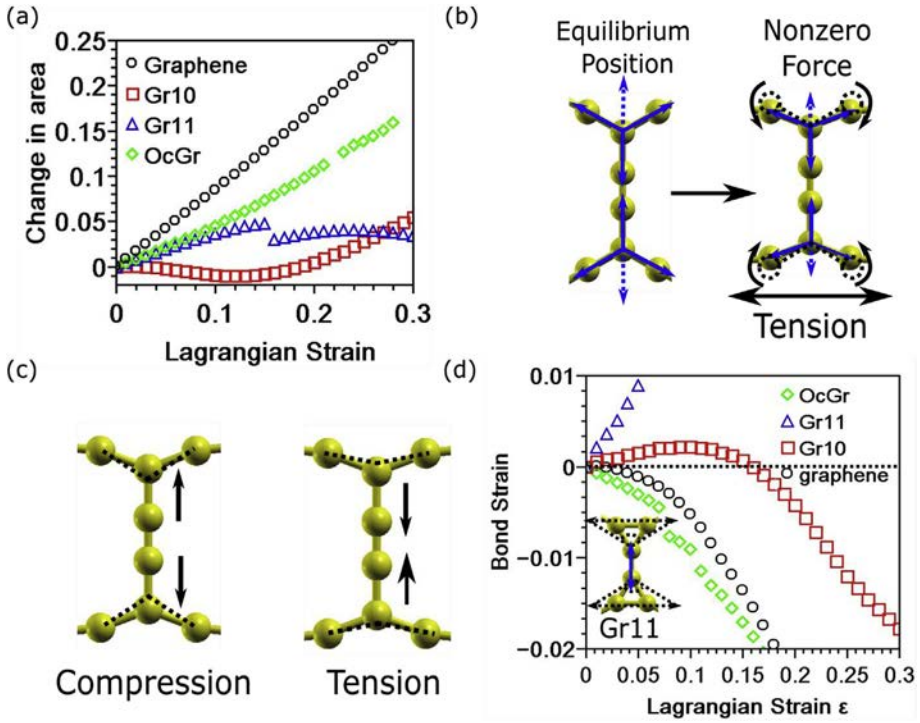

Fig. 3. The force equilibrium on the transverse direction during uniaxial tension. (a) The ratio between the area of the unit cell at the deformed states and the initial state of four carbon-based 2D structures during free-boundary uniaxial tension. (b) Part of the unit cell of Gr10 is used to illustrate the force equilibrium during the free-boundary uniaxial tension. Blue arrows represent the force direction, and dashed lines represent the initial position of bonds. (c) The two methods to reach a new force equilibrium by either compressing or stretching the bond perpendicular to the loading axis. (d) The strain of covalent bonds highlighted by red in Fig. 2(a) and perpendicular to the loading direction. Also, part of the unit cell of Gr11 is shown to illustrate the geometrical confinement of the three-atom ring. (A colour version of this figure can be viewed online.)

more profound, structural question: how does the deformed structure retain a free-boundary condition in the transverse direction during deformation? Since the component bond force of the stretched and rotated bonds reduces in the transverse direction, the original force balance in this direction is off if bonds perpendicular to the loading axis remain unchanged (Fig. 3(b)). Thus, a new force equilibrium must be obtained by either compressing or stretching the bond perpendicular to the loading direction (Fig. 3(c)). Tensile strains increase the rotation degree while compressive strains do the opposite. The strains of bonds perpendicular to the loading direction (bonds colored by red in Fig. 2(a)) at each applied strain value are plotted in Fig. 3(d), which shows that only bonds in Gr10 and Gr11 have tensile strain. Thus, bond rotation is suppressed in graphene, OcGr, and stanene but is promotive in Gr10 and Gr11, at least at the initial stage of deformation. As the applied strain increases to 0.12, the bond strain of Gr10 reaches the maximum positive value, and the area of Gr10 shrinks to its minimum value. When the bond strain becomes negative at 0.17, the strain-softening behavior of Gr10 initiates, a result of the suppression of bond rotation and dominance of bond stretch.

Different from all other four structures, Gr11 has a positive bond strain perpendicular to the loading axis throughout the deformation process (Fig. 3(d)). This abnormal behavior is attributed to the geometrical confinement of the atomic triangle in Gr11. Theoretically, all atomic rings having more than three atoms can be readily deformed solely by bond rotation, whereas the atomic triangle is inherently rigid: any bond rotation in it inevitably leads to bond stretch. Consequently, instead of releasing bond strain, bond rotation in the atomic triangle within Gr11 intensifies bond stretching (Fig. 3(d)), leading to a premature fracture and a lower UTS than that of Gr10 and OcGr (Fig. 1(c)). Accordingly, the deformation mechanisms of graphene allotropes are determined by not only the largest atomic ring but also the topological constraints of other smaller atomic rings, especially atomic triangles.

3.3. Bond-force-bond-strain relations of covalent bonds

Besides the effect of bond rotation on mechanical properties, is it possible for graphene allotropes to break this traditional cohesive strength limit with only bond stretch? If so, such a graphene allotrope much be composed of covalent bonds of which the bond strength S are larger than $K/10$, where K is the bond stiffness. To answer this question, uniaxial tension of 12 different covalent bonds in stanene, carbyne [32], graphene, OcGr, Gr11, Gr10, SqGr13 [24], Pentahexoctite (PHexOct) [33], and diamond were simulated (Fig. 4(a)). In our simulations, the strain was applied only to the tested bonds while atoms belonging to the other bonds were frozen; the bond energy corresponding to different strains was obtained by SCF calculations. The bond force $P(\varepsilon)$ acting on the stretched bond was calculated as the increasing rate of bond energy with bond strains $P(\varepsilon) = dE(\varepsilon)/d\varepsilon$.

Like the stress-strain responses of graphene allotropes, bond-force versus bond-strain responses perpetually deviate from linearity (Fig. 4(b)), reaches the tensile strength when the curve levels off, and then gradually decreases. The pseudo-ductile behavior of covalent bonds seems to contradict with the brittle fracture of Gr10 and Gr11 (Fig. 1(c)), of which stress sharply falls at the fracture strain. Such a brittle fracture is originated from strain-driven, structural transformations, which is discussed in Supporting Information Section 2. Herein, bond stiffness K is calculated as $K = \lim_{\varepsilon \to 0} d P(\varepsilon)/d\varepsilon$; the bond strength ($S$) of each bond was defined as the tensile strength of its force-strain curve. According to our hypothesis, K/S should be lower than 9 for some covalent bonds. However, the values of K/S for all covalent bonds are approximately equal to 9

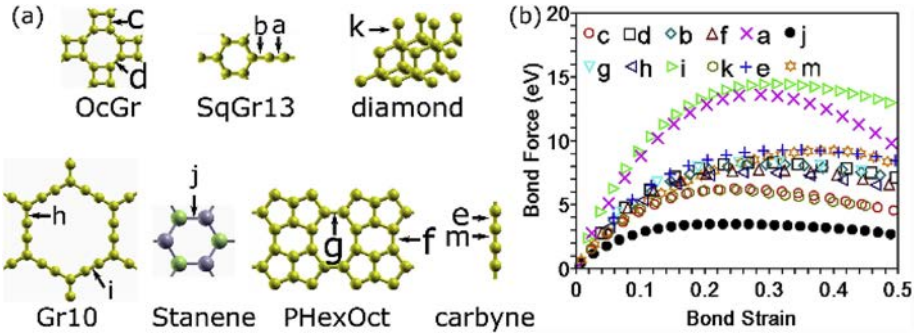

Fig. 4. Tension of 12 covalent bonds. The 12 covalent bonds tested here are labeled by letters in subfigure a. Their force-strain curves are shown in subfigure b. (A colour version of this figure can be viewed online.)

(Table 1), matching with the traditional theoretical cohesive strength limit.

3.4. Charge-density analysis of covalent bonds

To understand the physical insight behind the nearly identical K/S of all the tested 12 covalent bonds, we analyzed the charge density distribution along these bonds. According to the theory developed by Bader [34–36] and other authors [37], a covalent bond is formed as the charge density $\rho(r)$ accumulates along the bond path between the two bonded atoms (Fig. 5(a)). The mutual boundary between two atomic volumes intersects this line of concentrated charge density at a saddle point r_C, where the $\rho(r_C)$ of both sp^2- and sp^3-hybridized bonds attains a local minimum along the bond path but is maximum along transverse directions [34–36] (Fig. 5(b)). The charge density distribution in sp bonds, however, is different from that in sp^2 and sp^3 bonds. For example, in SqGr13, the bond A-B and C-D are sp^2-hybridized while B–C is sp-hybridized (Fig. 5(c)). In the sp bond B–C, since no saddle point exists, we define the bond critical point as the middle point between atom B and C, where $\rho(r_C)$ is the maximum in all directions (Fig. 5(d)). Additionally, due to the nearby sp bond, the saddle point along the sp^2 bond A-B is not at the center of the bond but close to atom A.

$\rho(r_C)$ is an important parameter in determining the bond force for it is proportional to the force exerted on the bonding electrons by the nuclei [37]. In this work, we found that the $\rho(r_C)$ of all the carbon-carbon covalent bonds labeled by letters in Fig. 4(a) share a universal relationship with their initial bond lengths L_0 (Fig. 6(a)).

Table 1
Mechanical properties of 12 covalent bonds labeled by letters in Fig. 4(a). K and S are the bond stiffness and bond strength of each bond. L_0 is the initial length. ε_{UTS} is the strain corresponding to UTS. ε_B is the strain defined by Eq. (6). ε_L is the strain when the Laplacian of the charge density at saddle points is zero ($\nabla^2\rho(r_C) = 0$).

	K(eV)	S(eV)	K/S	L_0 (Å)	ε_{UTS}	ε_B	ε_L
a	112.8	13.59	8.3	1.23	0.29	0.28	0.45
b	74.95	8.13	9.22	1.38	0.29	0.27	0.42
c	61.22	6.19	9.89	1.48	0.26	0.25	0.31
d	79.95	8.31	9.62	1.35	0.29	0.29	0.41
e	80.51	9.28	8.68	1.32	0.34	0.33	0.3
f	81.33	8.31	9.78	1.42	0.27	0.28	0.43
g	75.68	7.72	9.81	1.37	0.28	0.29	0.34
h	69.83	7.54	9.26	1.4	0.28	0.27	0.35
i	120.3	14.42	8.34	1.23	0.31	0.31	0.36
j	45.15	3.41	13.2	2.74	0.26	0.24	0.18
k	67.16	6.14	10.9	1.55	0.23	0.23	0.41
m	64.2	9.2	7	1.25	0.39	0.36	0.27

Such a relationship is also suitable for the $\rho(r_C)$ and L_0 of the carbon-carbon bond in ethylene [37], benzene [37], ethane [37], and cyclopropane [37]. Moreover, for stretched bonds, such as the stretched sp bond in Gr10 and sp^2 bond in OcGr in Fig. 4(a), the relationship between their elongated bond lengths and the corresponding $\rho(r_C)$ also overlaps with that between $\rho(r_C)$ and L_0. Not only is the relationship between the value of $\rho(r_C)$ and the corresponding bond lengths suitable for all carbon-carbon covalent bonds, but also the charge density distribution of different bonds near r_C would become similar if they were stretched to the same length. For example, in Fig. 6(b), we plotted the charge density distribution of an sp bond in Gr10 (the bond 'i' in Fig. 4(a)) and an sp^2 bond in OcGr (the bond 'd' in Fig. 4(a)) stretched to the same length of 1.56 Å. Along the three directions shown in Fig. 5(a), the two bonds share a common charge density distribution. Specifically, different from the charge density distribution of the relaxed sp bonds (Fig. 5(d)), a local minimum of the charge density along the bond path (Direction 1) is formed in the stretched sp bond (Fig. 6(b)), a distribution identical to that of the sp^2 bond stretched to the same length.

Since all carbon-carbon covalent bonds share a universal relation between their bond lengths and the charge density distribution near the bond critical point r_C, the difference in the initial bond length can be viewed as different initial strains ε_0. If we apply such initial strains ε_0 of different bonds to their force-strain curves, the original force-strain curves of all carbon-carbon covalent bonds can overlap each other into a universal force-strain relationship (Fig. 6(c)), which can be expressed in a Taylor series of strains as follows [12].

$$P(\varepsilon) = A_1\varepsilon + A_2\varepsilon^2 + A_3\varepsilon^3 + A_4\varepsilon^4 + \ldots \tag{2}$$

where $A_i, i = 1, 2, 3\ldots$ are fitting coefficients. Depending on the value of ε_0, K of different bonds can be written as $\lim_{\varepsilon\to\varepsilon_0} dP(\varepsilon)/d\varepsilon$. Based on this universal force-strain curve, the bond strength P of different bond is $P = P_{univ} - P(\varepsilon_0)$, where P_{univ} is the UTS corresponding to the universal force-strain curve $P(\varepsilon)$ and ε_0 is the initial strain of the bond. According to Eq. (2), K/S is given by

$$\frac{K}{S} = \frac{\lim_{\varepsilon\to\varepsilon_0} dP(\varepsilon)/d\varepsilon}{P_{univ} - P(\varepsilon_0)} = \frac{A_1 + 2A_2\varepsilon_0 + 3A_3\varepsilon_0^2 + 4A_4\varepsilon_0^3 + \ldots}{P_{univ} - A_1\varepsilon_0 - A_2\varepsilon_0^2 - A_3\varepsilon_0^3 - A_4\varepsilon_0^4 - \ldots} \tag{3}$$

For small values of ε_0, Eq. (3) becomes independent of ε_0.

$$\lim_{\varepsilon_0\to 0}\frac{K}{S} = \frac{A_1}{P_{univ}} \approx 9 \tag{4}$$

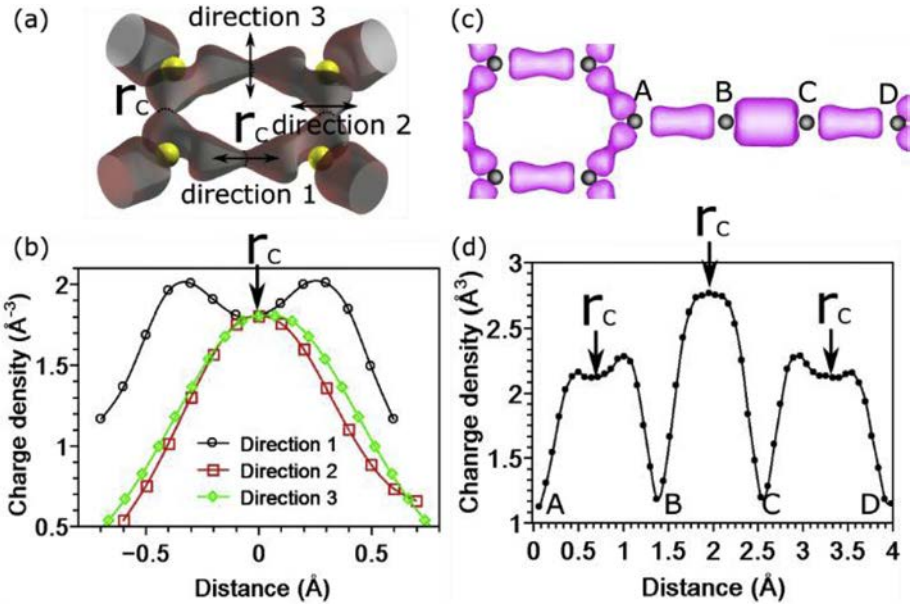

Fig. 5. Charge-density distribution near covalent bonds. (a) A Charge-density isosurface with a value of 1.68 Å^{-3} in OcGr is used to show the bond structure, the bond critical point r_C, and the three directions used to study charge-density distribution. (b) Charge-density distribution near r_C in the three directions illustrated in subfigure a. The horizontal coordinate represents the distance from r_C. (c) A charge-density isosurface with a value of 1.68 Å^{-3} in SqGr13 is used to show the difference between charge-density distribution along sp bonds and that along sp^2 bonds. (d) Charge-density distribution near r_C along the direction A→B→C→D. All data points are simulation results, and curves are fitting curves connecting discrete data points. (A colour version of this figure can be viewed online.)

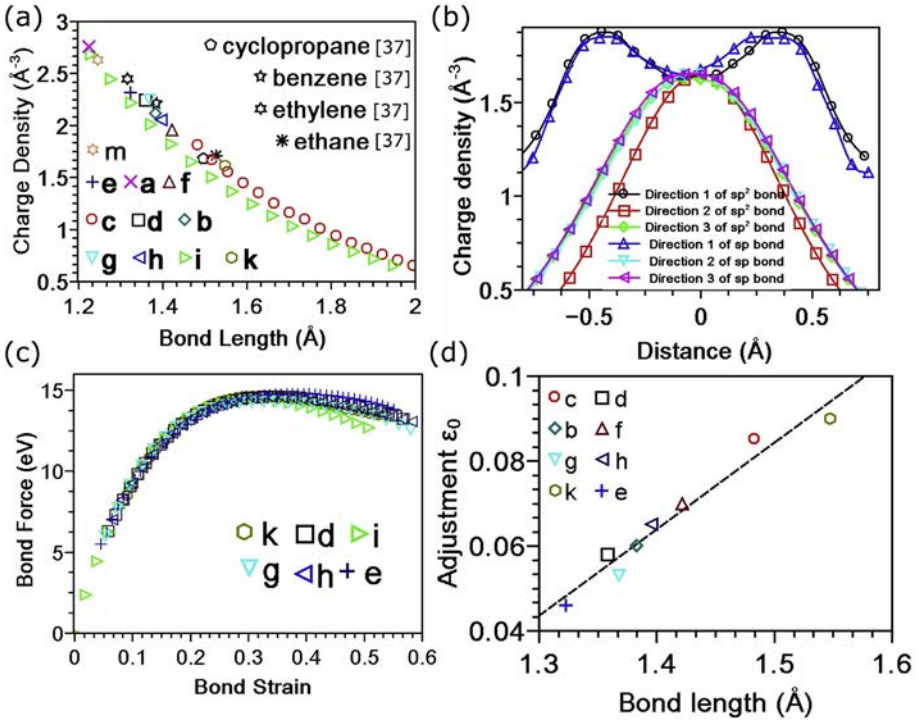

Fig. 6. A universal relationship between the charge-density evolution and bond force of covalent bonds. (a) The relationship between charge density at saddle points $\rho(r_C)$ and bond lengths, including both the initial length and stretched length. (b) The charge density distribution along the same three directions illustrated in Fig. 3(a) near the r_C of two bonds, "i" and "d", labeled in Fig. 4(a), stretched to the same length of 1.56 Å. (c) The universal force-strain curve valid for all carbon-carbon covalent bonds after adjustments of initial strains ε_0 based on their initial bond lengths. (d) The relationship between bond lengths and the initial strains ε_0. (A colour version of this figure can be viewed online.)

When ε_0 is smaller than 0.1, the values of K/S are approximately equal to 9. In the range of the initial bond lengths (1.22 Å to 1.55 Å), the charge density decreases linearly with increasing bond lengths, resulting in a linear relation between ε_0 and bond lengths (Fig. 6(d)). Even for the maximum adjustment, 0.09 of sp^3 bonds in diamond, Eq. (4) is still valid. Thus, K/S of all the carbon-carbon

covalent bonds are approximately 9.

3.5. The fracture mechanism of different covalent bonds

Although the UTS of the force-strain curve of each bond is treated as its bond strength, the force after UTS points did not drop abruptly, exhibiting a pseudo-ductile behavior. Thus, the fracture mechanism of the covalent bond has not yet been fully developed. It is possible that the mechanical integrity of an atomic bond might still hold after its UTS point. Since the charge density at r_C is the minimum along the bond path, the disintegration of a bond always initiates from r_C. The critical bond-breaking strain is often determined by the Laplacian of the charge density at r_C ($\nabla^2\rho(r_C)$) [34–36] because $\nabla^2\rho(r_C)$ of any scalar field is negative where the scalar field is a concave function of the position. For example, in the one-dimensional case

$$\begin{aligned}&\lim_{\Delta x\to 0}\{\rho(x)-1/2[\rho(x-\Delta x)+\rho(x+\Delta x)]\}\\&=-1/2\lim_{\Delta x\to 0}\{[\rho(x+\Delta x)-\rho(x)]-[\rho(x)-\rho(x-\Delta x)]\}\\&=-1/2d^2\rho(x)/dx^2\end{aligned}\tag{5}$$

When $d^2\rho(x)/dx^2<0$, $\rho(x)>(\rho(x+\Delta x)+\rho(x-\Delta x))/2$, the value of $\rho(x)$ is larger than the average value of its neighbors, a result of the concentration of electrons at the point x. In a 3D space, $\nabla^2\rho(r)$ is calculated by summing up the three eigenvalues of the Hessian matrix of charge density $H(\rho(r))$,

$$H(\rho(r))=\begin{bmatrix}\frac{\partial^2\rho(r)}{\partial x\partial x} & \frac{\partial^2\rho(r)}{\partial x\partial y} & \frac{\partial^2\rho(r)}{\partial x\partial z}\\ \frac{\partial^2\rho(r)}{\partial y\partial x} & \frac{\partial^2\rho(r)}{\partial y\partial y} & \frac{\partial^2\rho(r)}{\partial y\partial z}\\ \frac{\partial^2\rho(r)}{\partial z\partial x} & \frac{\partial^2\rho(r)}{\partial z\partial y} & \frac{\partial^2\rho(r)}{\partial z\partial z}\end{bmatrix}\tag{6}$$

where x, y, and z are three orthogonal space vectors. The three eigenvectors corresponding to the three eigenvalues $\lambda_1,\lambda_2,\lambda_3$ are labeled as direction 1, direction 2, and direction 3, respectively. As shown in Fig. 5(a), direction 1 is along the bond path; direction 2 lies on the atomic plane of graphene allotropes and is perpendicular to the bond path; direction 3 is perpendicular to the atomic plane. To analyze the evolution of the three eigenvalues during bond stretching, we plotted in Fig. 7(a) the relation between the three eigenvalues and bond lengths for the sp^2 bond 'c' (1.48 Å), bond 'd' (1.35 Å) in OcGr, and the sp bond 'm' in carbyne (1.23 Å). For all the three bonds, λ_3 and λ_2 are always negative and converge to zero at an infinite bond length; accordingly, electrons always concentrate at r_C in the two directions perpendicular to the bond path. λ_1 is always positive for sp^2 bonds, reflecting the structure of the saddle point at r_C (Fig. 5(c)); however, λ_1 is initially negative for sp bonds, matching with the maximum charge density in all directions at r_C of sp bonds (Fig. 5(d)). As bond lengths increase, λ_1 first increases but finally decreases as all eigenvalues converge to zero at infinite bond lengths.

Since $\nabla^2\rho(r_C)$ is the sum of the three eigenvalues λ_1, λ_2, λ_3, $\nabla^2\rho(r_C)$ is less than zero when $|\lambda_3|+|\lambda_2|>\lambda_1$, and the charge density concentrates at r_C; otherwise, the charge density disperses at r_C. In Fig. 7(b), we plotted $\nabla^2\rho(r_C)$ and the corresponding initial bond lengths of all the 16 bonds shown in Fig. 4(a), as well as $\nabla^2\rho(r_C)$ and bond lengths during bond stretching. Generally, $\nabla^2\rho(r_C)$ increases with bond lengths but gradually ceases to increase when $\nabla^2\rho(r_C)$ is larger than zero. The point at which $\nabla^2\rho(r_C)$ becomes positive is always regarded as the bond-breaking point because after this point electrons do not concentrate at r_C anymore [37]. Consequently, the strain at which $\nabla^2\rho(r_C)=0$ (ε_L) should be equal to the strain corresponding to UTS (ε_{UTS}). However, for most of the bonds studied here, ε_L are found to be larger than ε_{UTS} (Table 1); electrons continue to accumulate at r_C after UTS points. Therefore, it is inaccurate to use the strain at which $\nabla^2\rho(r_C)=0$ (ε_L) to explain the bond-fracture mechanism of covalent bonds and estimate the strain corresponding to UTS.

Except for the physical criterion based on $\nabla^2\rho(r)$, a commonly accepted mechanical definition of the UTS point is the initiation of necking. Since the force exerted on the bonding electrons by the nuclei is proportional to $\rho(r_C)$, we obtain

$$\begin{aligned}\left.\frac{dP}{d\varepsilon}\right|_{\varepsilon=\varepsilon_B}&=\left.\frac{d(\rho(r_C)\sigma(r_C))}{d\varepsilon}\right|_{\varepsilon=\varepsilon_B}=\rho(r_C)\frac{d\sigma(r_C)}{d\varepsilon}+\sigma(r_C)\frac{d\rho(r_C)}{d\varepsilon}\\&=0,\ \frac{d\sigma(r_C)}{\sigma(r_C)d\varepsilon}=-\frac{d\rho(r_C)}{\rho(r_C)d\varepsilon}\end{aligned}\tag{7}$$

$d\sigma(r_C)/d\varepsilon$ captures the hardening behavior due to the increasing potential energy per electron with strains while $d\rho(r_C)/d\varepsilon$ signifies the softening due to the decreasing $\rho(r_C)$ with strain. When the physical-hardening effect overwhelms the geometrical-softening effect, deformation proceeds in a stable mode. The external load must increase to introduce further deformation of the covalent bond. As the bond length increases, however, the hardening coefficient $d\sigma(r_C)/d\varepsilon$ decreases with strain (Fig. 7(c)). Consequently, a critical strain (ε_B) is reached at which the effect of physical hardening and geometrical softening balances. At even larger strain, the physical-hardening effect cannot compensate the geometrical-softening effect anymore, and the external load will decrease but because of the diminishing charge density at the saddle point (Fig. 7(d)). The calculated balancing point ε_B according to Eq. (7) is very close to ε_{UTS} (Table 1). The absolute error between ε_{UTS} and ε_B is within 7.7%, and the mean error is 3.2%, affirming the validity of our explanation on the bond fracture mechanism and approximation of UTS points.

4. Conclusions

In summary, we showed that bond rotation plays a significant role in the deformation of graphene allotropes with high Poisson's ratios. As a result, graphene allotropes with Poisson's ratios close to 0.8, such as Gr10, have an S-shape stress-strain curve with UTS ($E/UTS\approx 1.7$), exceeding the traditional theoretical cohesive strength limit $E/UTS\approx 10$. Such a deformation mechanism usually belongs to elastomers like polyurethane. However, the Young's modulus and UTS of polyurethane are much smaller than that of Gr10. Further analysis found that the deformation of Gr10 is dominated by bond rotations initially and then by bond stretch at large strains, thereby increasing the fracture strain. Besides the influence of bond rotation, in-depth analysis of the deformation of covalent bonds indicates that the force-strain curves of all bonds follow an identical bond-force vs. bond-strain relation after accounting for initial strains owing to the differences in initial bond lengths. Therefore, all carbon-carbon bonds share a constant ratio between bond stiffnesses K and bond strengths S ($K/S\approx 9$). The charge-density analysis elucidates the reasons why the traditional cohesive strength limit $E/UTS\approx 10$ is suitable for brittle materials deformed mainly by bond stretch. Overall, this study suggests how an exciting interplay between bond stretching and bond rotation can enhance the fracture strains of graphene allotropes.

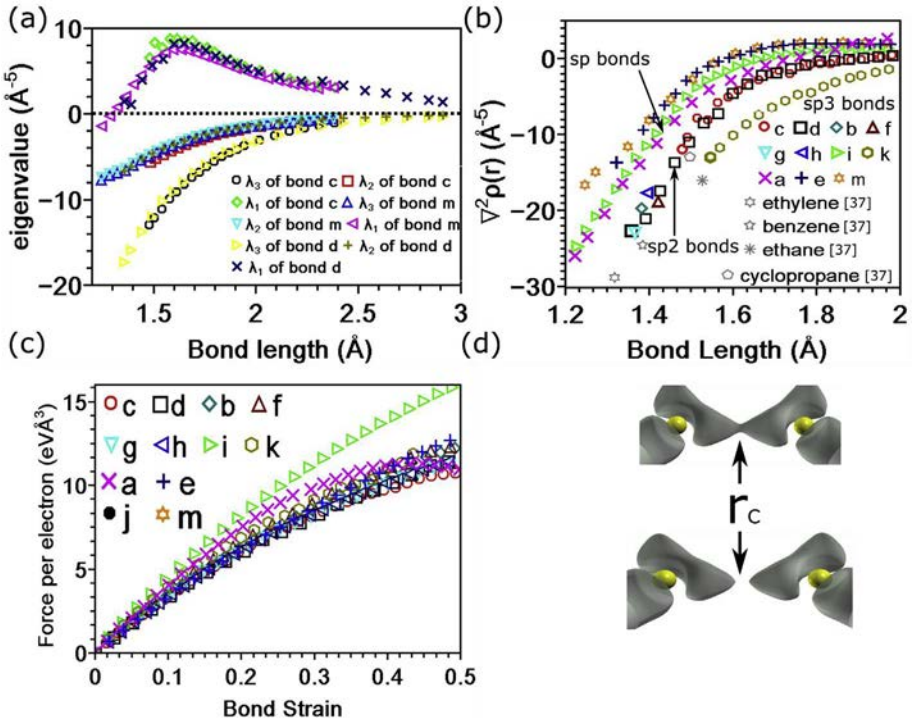

Fig. 7. The fracture of covalent bonds by the necking of charge density. (a) The relationship between the three eigenvalues of the Hessian matrix of the charge density at saddle points $H(\rho(r_C))$ and bond lengths. (b) The relationship between $\nabla^2\rho(r_C)$ and bond lengths, including both the initial lengths and the stretched lengths of bond "k", "m", "e", "i", "a", "c", and "d" in Fig. 4(a). (c) The relationship between bond force per electron at saddle points $\sigma(r_C)$ and bond strains. (d) A Charge-density isosurface with a value of 1.68 Å^{-3} is used to illustrate the decreasing charge density at r_C along the bond path. (A colour version of this figure can be viewed online.)

Acknowledgments

Financial support for this work was provided in-parts by the Natural Sciences and Engineering Research Council of Canada, Hart Professorship, the Ontario Research Foundation, Ontario Graduate Scholarship (OGS), and the Mitacs. The computational resources were provided by the SciNet consortium through the Compute Canada resource allocations.

Appendix A. Supplementary data

Supplementary data to this article can be found online at https://doi.org/10.1016/j.carbon.2018.11.079.

References

[1] A.A. Griffith, The phenomena of rupture and flow in solids, Philos. Trans. R. Soc. Lond. - Ser. A Contain. Pap. a Math. or Phys. Character (1921) 163–198.
[2] E. Orowan, Fracture and strength of solids, Rep. Prog. Phys. 12 (1949) 185–232, https://doi.org/10.1088/0034-4885/12/1/309.
[3] A. Kelly, N.H. Macmillan, Strong Solids, third ed., Clarendon Press, Oxford [Oxfordshire], 1986.
[4] A. Cottrell, The Mechanical Properties of Matter, Krieger Pub. Co, Huntington, N.Y, 1981.
[5] A.S. Tetelman, A.J. McEvily, Fracture of Structural Materials, Wiley, New York, 1967.
[6] A. Kelly, W.R. Tyson, A.H. Cottrell, Ductile and brittle crystals, Philos. Mag. A 15 (1967) 567–586, https://doi.org/10.1080/14786436708220903.
[7] R. Peierls, The size of a dislocation, Proc. Phys. Soc. 52 (1940) 34–37, https://doi.org/10.1088/0959-5309/52/1/305.
[8] F.R.N. Nabarro, Dislocations in a simple cubic lattice, Proc. Phys. Soc. 59 (1947) 256–272, https://doi.org/10.1088/0959-5309/59/2/309.
[9] L.M. Brown, G.R. Woolhouse, U. Valdrè, Radiation-induced coherency loss in a Cu–Co alloy, Philos. Mag. A 17 (1968) 781–789, https://doi.org/10.1080/14786436808223029.
[10] C. Lee, X. Wei, J.W. Kysar, J. Hone, Measurement of the elastic properties and intrinsic strength of monolayer graphene, Science 321 (2008) 385–388, https://doi.org/10.1126/science.1157996.
[11] S. Bertolazzi, J. Brivio, A. Kis, Stretching and breaking of ultrathin MoS $_2$, ACS Nano 5 (2011) 9703–9709, https://doi.org/10.1021/nn203879f.
[12] C. Cao, M. Daly, C.V. Singh, Y. Sun, T. Filleter, High strength measurement of monolayer graphene oxide, Carbon 81 (2015) 497–504, https://doi.org/10.1016/j.carbon.2014.09.082.
[13] X. Wei, B. Fragneaud, C.A. Marianetti, J.W. Kysar, Nonlinear elastic behavior of graphene: *Ab initio* calculations to continuum description, Phys. Rev. B 80 (2009), https://doi.org/10.1103/PhysRevB.80.205407.
[14] H. Wang, Q. Li, Y. Gao, F. Miao, X.-F. Zhou, X.G. Wan, Strain effects on borophene: ideal strength, negative Possion's ratio and phonon instability, New J. Phys. 18 (2016), 073016, https://doi.org/10.1088/1367-2630/18/7/073016.
[15] Q. Peng, C. Liang, W. Ji, S. De, A first-principles study of the mechanical properties of g-GeC, Mech. Mater. 64 (2013) 135–141, https://doi.org/10.1016/j.mechmat.2013.05.009.
[16] Z. Shi, C.V. Singh, The ideal strength of two-dimensional stanene may reach or exceed the Griffith strength estimate, Nanoscale 9 (2017) 7055–7062, https://doi.org/10.1039/C7NR00010C.
[17] S. Das, S. Mojumder, T. Rakib, M.M. Islam, M. Motalab, Atomistic insights into mechanical and thermal properties of stanene with defects, Phys. B Condens. Matter 553 (2019) 127–136, https://doi.org/10.1016/j.physb.2018.10.035.
[18] H. Sun, S. Mukherjee, C.V. Singh, Mechanical properties of monolayer pentagraphene and phagraphene: a first-principles study, Phys. Chem. Chem. Phys. 18 (2016) 26736–26742, https://doi.org/10.1039/C6CP04595B.
[19] H. Sun, S. Mukherjee, M. Daly, A. Krishnan, M.H. Karigerasi, C.V. Singh, New insights into the structure-nonlinear mechanical property relations for graphene allotropes, Carbon 110 (2016) 443–457, https://doi.org/10.1016/j.carbon.2016.09.018.
[20] P. Giannozzi, S. Baroni, N. Bonini, M. Calandra, R. Car, C. Cavazzoni, D. Ceresoli, G.L. Chiarotti, M. Cococcioni, I. Dabo, A. Dal Corso, S. de Gironcoli, S. Fabris, G. Fratesi, R. Gebauer, U. Gerstmann, C. Gougoussis, A. Kokalj, M. Lazzeri, L. Martin-Samos, N. Marzari, F. Mauri, R. Mazzarello, S. Paolini, A. Pasquarello, L. Paulatto, C. Sbraccia, S. Scandolo, G. Sclauzero, A.P. Seitsonen, A. Smogunov, P. Umari, R.M. Wentzcovitch, QUANTUM ESPRESSO: a modular and open-source software project for quantum simulations of materials, J. Phys. Condens. Matter 21 (2009), 395502, https://doi.org/10.1088/0953-8984/21/39/395502.
[21] J.P. Perdew, K. Burke, M. Ernzerhof, Generalized gradient approximation made simple, Phys. Rev. Lett. 77 (1996) 3865–3868, https://doi.org/10.1103/PhysRevLett.77.3865.
[22] H.J. Monkhorst, J.D. Pack, Special points for Brillouin-zone integrations, Phys. Rev. B 13 (1976) 5188–5192, https://doi.org/10.1103/PhysRevB.13.5188.
[23] X.-L. Sheng, H.-J. Cui, F. Ye, Q.-B. Yan, Q.-R. Zheng, G. Su, Octagraphene as a versatile carbon atomic sheet for novel nanotubes, unconventional fullerenes,

and hydrogen storage, J. Appl. Phys. 112 (2012), 074315, https://doi.org/10.1063/1.4757410.
[24] A.N. Enyashin, A.L. Ivanovskii, Graphene allotropes, Phys. Status Solidi B 248 (2011) 1879–1883, https://doi.org/10.1002/pssb.201046583.
[25] R.H. Baughman, H. Eckhardt, M. Kertesz, Structure-property predictions for new planar forms of carbon: layered phases containing sp2 and sp atoms, J. Chem. Phys. 87 (1987) 6687, https://doi.org/10.1063/1.453405.
[26] F. Liu, P. Ming, J. Li, *Ab initio* calculation of ideal strength and phonon instability of graphene under tension, Phys. Rev. B 76 (2007), https://doi.org/10.1103/PhysRevB.76.064120.
[27] Q. Peng, W. Ji, S. De, Mechanical properties of graphyne monolayers: a first-principles study, Phys. Chem. Chem. Phys. 14 (2012), 13385, https://doi.org/10.1039/c2cp42387a.
[28] X.-Q. Wang, H.-D. Li, J.-T. Wang, Prediction of a new two-dimensional metallic carbon allotrope, Phys. Chem. Chem. Phys. 15 (2013) 2024–2030, https://doi.org/10.1039/C2CP43070C.
[29] Z.M. Huang, S. Ramakrishna, A.A.O. Tay, Modeling the stress/strain behavior of a knitted fabric-reinforced elastomer composite, Compos. Sci. Technol. 60 (2000) 671–691, https://doi.org/10.1016/S0266-3538(99)00164-5.
[30] U.A. Pinto, L.L.Y. Visconte, R.C. Reis Nunes, Mechanical properties of thermoplastic polyurethane elastomers with mica and aluminum trihydrate, Eur. Polym. J. 37 (2001) 1935–1937, https://doi.org/10.1016/S0014-3057(01)00069-6.
[31] A. Fujinami, S. Ogata, Y. Shibutani, Ab initio study of the tensile behavior of single polyimide molecular chain, Polymer 45 (2004) 9023–9028, https://doi.org/10.1016/j.polymer.2004.10.058.
[32] M. Liu, V.I. Artyukhov, H. Lee, F. Xu, B.I. Yakobson, Carbyne from first principles: chain of C atoms, a nanorod or a nanorope, ACS Nano 7 (2013) 10075–10082, https://doi.org/10.1021/nn404177r.
[33] B.R. Sharma, A. Manjanath, A.K. Singh, pentahexoctite, A new two-dimensional allotrope of carbon, Sci. Rep. 4 (2014) 7164, https://doi.org/10.1038/srep07164.
[34] R.F.W. Bader, A quantum theory of molecular structure and its applications, Chem. Rev. 91 (1991) 893–928, https://doi.org/10.1021/cr00005a013.
[35] R.F.W. Bader, From Schrodinger to atoms in molecules, Pure Appl. Chem. 60 (1988), https://doi.org/10.1351/pac198860020145.
[36] R.F.W. Bader, H. Essén, The characterization of atomic interactions, J. Chem. Phys. 80 (1984) 1943–1960, https://doi.org/10.1063/1.446956.
[37] D. Cremer, E. Kraka, A description of the chemical bond in terms of local properties of electron density and energy, Croat. Chem. Acta. 57 (n.d.) 1259–1281.